Yang Gao · Bin Li · Han Zhang · Weile Wu · Jun Li · Yueping Yin

Numerical modeling of mixed two-phase in long runout flow-like landslide using LPF3D

Abstract Under extreme climate conditions, such as heavy precipitation, glacial lake outbursts, and ice and snow melting, the long runout flow-like landslide with mixed solid–liquid two-phase has become one of the most disastrous types in the world. Numerical simulation is one of the most important means in disaster prevention and mitigation work for this type of landslide. In this study, a new full three-dimensional landslide post-failure numerical platform (LPF^{3D}) was proposed. This method serves as a bridge between continuum-medium algorithms and discrete-medium algorithms based on the same theoretical numerical framework of smoothed particle hydrodynamics (SPH). This computational model employs an elastic-viscoplastic constitutive law and basal resistance of frictional model for the solid grain phase, and the fluid phase is treated as a Newtonian fluid. A drag law describes the interaction stress between fluid and grain. The boundary normal forces were applied using the penalty function method to ensure the stability of the algorithm. Comparison analyses of small-scale flume experiments and realistic-scale landslide cases and different numerical methods were performed to show that this numerical modeling is capable of simulating mixed two-phase flow. This new method realizes the actual physical and mechanical action process of mixed two-phase flow with higher computational efficiency, and is an appropriate benchmark for the post-failure risk forecasting and assessment of long runout flow-like landslide.

Keywords Long runout landslide · Flume experiments · Mixed two-phase flow · Drag force · LPF^{3D}

List of symbols

ξ	Volume fraction
ρ	Density
v	Velocity
R_{fp}	Interaction force between solid and liquid phases
P	Pressure
σ	Total stress
τ	Friction stress
c_0	Initial velocity of sound
ε	Friction strain rate
μ	Viscosity coefficient
V_P	Average volume
M_P	Average mass
m	Mass
$\dot{\sigma}$	Incremental form of the stress component
G	Friction modulus
K	Elastic modulus
E	Young's modulus
$\dot{e}$	Deviatoric friction strain rate tensor
$\dot{\epsilon}$	Strain rate tensor
β	Momentum transfer coefficient between the fluid and solid
C_D	Traction coefficient
μ_f	Fluid viscosity
d_P	Particle size of the solid
ρ_f	Fluid density
ξ_f	Fluid volume fraction
Re_P	Relative Reynolds number
ω	Penalty parameter
r	Radial vector
A	The area of boundary grain
r_u	Pore pressure coefficient
Φ	Friction angle
H	Fluid depth

Introduction

Long runout flow-like landslides with mixed solid–liquid two-phase often present a great danger to human life and property safety (Iverson 1997; Takarada 1999; Yin et al. 2011, 2016; Xing et al. 2017; Fan et al. 2019). Historically, this type of landslide has occurred many times around the world, such as the Yungay landslide in Peru in 1970 (Plafker and Erichsen 1978), the Kolka landslide in Russia in 2002 (Evans et al. 2009), the Leyte landslide in Philippines in 2007 (Evans et al. 2007), the Sanxicun landslide in Sichuan, China in 2013 (Yin et al. 2016; Gao et al. 2017), and the Shuicheng landslide in Guizhou, China in 2019 (Gao et al. 2020). Sliding main body is mixed by solid debris grains and ice/snow melt water or heavy precipitation leads to abundant surface runoff. Some good evidence has been obtained that single-phase dry debris avalanches can transform into mixed two-phase debris flows, and the involvement of fluid phase is critical in the long runout motion process (Voight et al. 1983; Iverson and LaHusen 1997; Mothes et al. 1998; Takarada et al. 1999). Risk forecasting and assessment have become the subject of considerable attention in the geological hazard research field, and numerical simulation methods play a significant role to solve this issue.

A series of mathematical and dynamics models were recorded involving open-channel mixed grain-liquid flows (Pudasaini and Mergili 2019; Liu et al. 2020, 2017; Shu et al. 2020; Shen et al. 2022; Yin et al. 2023; Singh et al. 2023). Two-phase flow analyzing problems are commonly described using either the mixture theory or the two-fluid theory (Ishii 1975). (i) The mixture theory provides a means for studying motions of bodies made up of several constituents by generalizing the equations and principles of the mechanics of a single continuum (Truesdell 1984; Bowen 1980; Johnson 1990; Kafui et al. 2002; Topin et al 2011). It more focused on the selection of the basal resistance model which

depends on the rheological parameters of the different material types (Savage and Hutter 1989, 1991; Iverson 2001; Pastor et al. 2015; Hungr 1995; Hungr and McDougall 2009; Voellmy 1955). The role of the fluid phase shows contribution mainly through the reduction of the friction coefficient at the substrate (Mencl 1966; Habib 1975; Sassa 1989, 1994; Savage and Iverson 2003; Iverson 2012). However, in fact the two-phase flow motion is an interaction process between the fluid phase and the solid phase, which have their respective physical and mechanical significance. (ii) The two-fluid theory considers the microscopic interactions between the two phases and derives the basic control equations for each phase, in which consists of two sets of conservation equations that govern the mass, momentum, and energy balance of each phase. It is important to provide a correlation for the interfacial force for the two-fluid theory (Ishii and Zuber 1979). Compared with the gas, the liquid affects the landslide movement more significantly. The existence of liquid leads to a decrease in the friction between solid grains, and causing the grains to enhance the mobility of sliding main body with the water pressure and interphase forces. A large number of studies have shown that the interphase forces between the solid phase and the fluid phase mainly include water pressure, drag forces, additional mass forces, Basset forces, etc., of which the water pressure is particularly critical (Stokes 1851; Ishii and Zuber 1979; Khan and Richardson 1987; Iverson 1997; Pudasaini 2012; Lee and Huang 2018; Tayyebi 2021; Tayyebi 2022; Gao et al. 2022).

To assess the risk quantitatively of long runout flow-like landslides post failure process, numerical methods are an efficient tool. Currently, a large number of studies have been carried out on different material types of sliding main body by discrete-medium methods and continuous-medium methods. These are summarized as follows: (i) Discrete medium methods have been used to simulate solid grain, such as discrete element method (DEM), which are mainly based on Newton's laws of motion and inter-grain contact models (e.g., EDEM and MatDEM) (Liu et al. 2017; Zhao et al. 2020). This type of method can visualize the interactions between particles, which has a simple theory and few assumptions. However, due to the large number of particles in a real particle flow problem, the amount of computation and the computation time required are enormous. (ii) In terms of continuous medium methods, grid algorithms and particle algorithms have been developed to study the fluid mobility by Euler and Lagrangian continuum fluid algorithms (e.g., finite volume method (FVM), smoothed particle hydrodynamics (SPH), lattice Boltzmann method (LBM), and material point method (MPM)). Continuous medium methods can calculate the state of motion as a whole, but each particle or particle–particle interaction cannot be accurately described in macro mechanical parameters. (iii) In order to explore the disaster motion process between different phases, it is necessary to adopt a multi-algorithm coupling method to complete this work. The coupling method of discrete-medium and continuous-medium algorithms is mostly to simulate the motion characteristics of the multi-phase flow, such as DEM-FVM and DEM-SPH coupling (Canelas et al. 2016; Shan et al. 2014; Tan and Chen 2017; Tan et al. 2018; Jing et al. 2019; Gao et al. 2022). Current two-phase coupling simulation methods can theoretically reflect the movement mechanism of solids and fluids better, but the number of particles required to ensure the accuracy of the simulation is high and the simulation efficiency is low.

In this study, a full three-dimensional numerical simulation method was established for the coupled two-phase flow-like landslide. This method serves as a bridge between continuum-medium algorithms and discrete-medium algorithms based on the same numerical theoretical framework of smoothed particle hydrodynamics (SPH). The smoothed discrete particle hydrodynamics (SDPH) method was used to simulate discrete medium grains, and the smoothed particle hydrodynamics (SPH) method was used to simulate continuous medium fluids, such as water and slurry. A novel and high-efficiency software platform was proposed by the first author and his team, called the three-dimensional landslide post-failure (LPF³ᴰ) method. The numerical modeling was verified using flume experiments and realistic landslide case and comparison of different numerical methods, and simulation results were consistent with the experiment and landslide case data. This method involving mixed two-phase flow dynamics modeling reflects the actual physical and mechanical action processes of long runout flow-like landslides, and it can be applied for post-failure risk forecasting and assessment.

Computational model

In this paper, smoothed particle hydrodynamics (SPH) and smoothed discrete particle hydrodynamics (SDPH) were used to solve the fluid and grains separately under the same theoretical numerical algorithm framework. The rheological and constitutive laws were based on an elastic-viscoplastic model for dense granular flow, and the interstitial fluid is treated as a Newtonian fluid. The drag force needs to focus on interphase action of mixed flow. The boundary forces were applied using the penalty function method to ensure the stability of the algorithm. A landslide post-failure software platform (LPF³ᴰ) was developed. LPF³ᴰ couples solid particles and fluids in full three-dimensional based on the macroscopic continuous medium algorithm framework (SPH), which features high computational efficiency and accuracy. The aim is able to simulate the post-failure process of different types of landslides.

Continuous phase

Researchers have proposed several Lagrangian particle methods (Lucy 1977; Gingold and Monaghan 1977). SPH is a complete Lagrangian particle method and offers excellent advantages in the simulation and mobility of fluid phase.

Conservation equations for the continuous phase
The mass and momentum conservation equations for the continuous phase f are, respectively, as follows:

$$\frac{\partial}{\partial t}\left(\xi_f \rho_f\right) + \nabla \cdot \left(\xi_f \rho_f \boldsymbol{v}_f\right) = 0, \tag{1}$$

$$\frac{\partial}{\partial t}\left(\xi_f \rho_f \boldsymbol{v}_f\right) + \nabla \cdot \left(\xi_f \rho_f \boldsymbol{v}_f \boldsymbol{v}_f\right) = -\xi_f \nabla P_f + \nabla \cdot \boldsymbol{\tau}_f + \boldsymbol{R}_{fp} + \xi_f \rho_f \boldsymbol{g}. \tag{2}$$

where ξ_f, ρ_f, and $\boldsymbol{v}_f$ are the volume fraction, density, and velocity of the fluid, respectively; $\boldsymbol{R}_{fp}$ is the interaction force between solid and liquid phases; P_f is the pressure of the dispersed phase; and $\boldsymbol{\tau}_f$ is the continuous phase viscous stress tensor.

Rheological and constitutive laws

This constitutive model is used to simulate water and high-concentration fluids based on weakly compressible fluid model (Monaghan 1994). The relationship between the fluid density and pressure P is.

$$P = P_0 \left[\left(\frac{\rho}{\rho_0} \right)^\gamma - 1 \right], \tag{3}$$

where $P_0 = \rho_0 c_0^2 / \gamma$, ρ_0 is the initial density of the fluid, γ is related to the compressibility of the fluid (herein, $\gamma = 7$), and c_0 is the initial speed of sound. In order to ensure compressibility of the fluid, c_0 should be in the range of $10 v_{max} - 40 v_{max}$, where v_{max} is the maximum velocity of the fluid.

For Newtonian fluids, the viscous shear stress τ is proportional to the shear strain rate ε and the fluid viscosity coefficient μ_f. τ and ε are defined as follows:

$$\tau = \mu_f \varepsilon, \tag{4}$$

$$\varepsilon = \nabla \cdot v + \nabla \cdot v^{\mathrm{T}} - \frac{2}{3} (\nabla \cdot v) \delta. \tag{5}$$

where for non-Newtonian fluids, the viscosity coefficient μ is a function of the shear strain rate. δ is the unit tensor.

Discrete phase

Numerical method-smoothed discrete particle hydrodynamics (SDPH)

Solving for the discrete grain phase has been improved as smoothed discrete particle hydrodynamics (SDPH), in which the new physical quantities characterized by one SDPH particle are added to traditional SPH parameters (Chen et al. 2017). The Lagrangian smoothed particle hydrodynamics method is based on macroscopic continuum mechanics, and SDPH method employs the Lagrangian particle method to obtain discrete solutions. Each individual particle can be traced with this approach, and its information can be obtained with low computational cost. In this paper, discrete particles as pseudo-fluids do not just consider the difference between the constitutive equations, and the pseudo-fluid region is also discretized.

The traditional continuum method of SPH was transformed into the discrete method of SDPH based on the volume fraction of the effective density in the macroscopic continuum algorithm framework (Pähtz et al. 2019; Kim and Kamrin 2020; Chen and Yan 2021). SDPH grains not only had various physical properties, such as masses, densities, velocities, and accelerations, but also various grain properties, such as grain sizes and volume fraction (Fig. 1). In this study, the grains were treated as a quasi-fluid of dense granular flow. The coupled numerical modeling of SPH and SDPH is better simulation in the pseudo-fluid regions based on volume fraction.
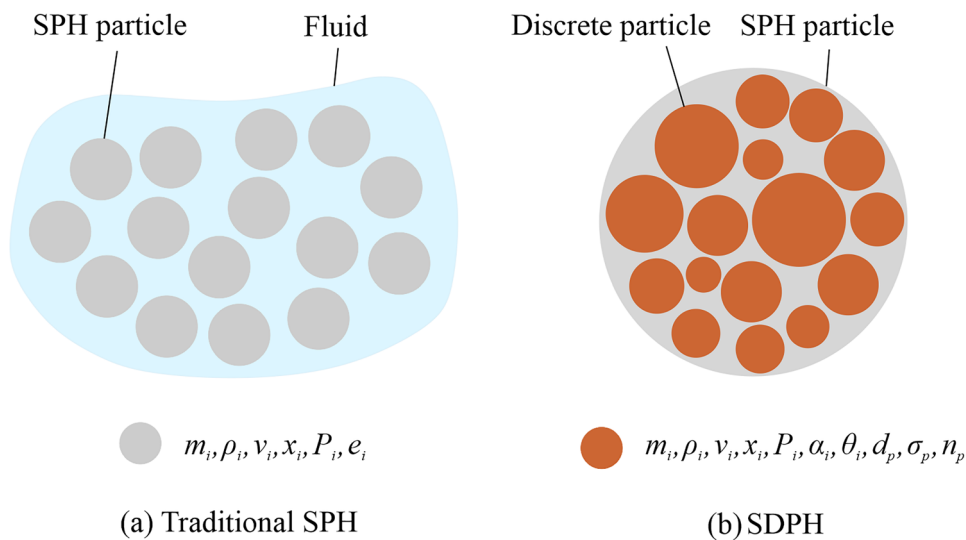
The relationship between the profiles of SPH particles and those of the discrete particles are also presented as follows:

$$\rho_{SPH} = \rho = \xi_P \rho_P, \tag{6}$$

where ρ_{SPH}, α_P, and ρ_P are the effective density of the SPH fluid, the volume fraction, and true density of the grain phase, respectively. If particles are found in the flow field, the average volume and mass are V_P and M_P, respectively, and the total volume of the space is V_0. Thus,

$$\rho_{SPH} = \xi_P \rho_P = \frac{n V_P}{V_0} \rho_P = \frac{n M_P}{V_0}. \tag{7}$$

The pseudo-fluid domain is discretized and solved for a series of particles using the SDPH method. The estimated value of the function $f(r_i)$ and its spatial derivative $\nabla \cdot f(r_i)$ for particle i are

SPH particle   Fluid

$m_i, \rho_i, v_i, x_i, P_i, e_i$

(a) Traditional SPH

Discrete particle   SPH particle

$m_i, \rho_i, v_i, x_i, P_i, \alpha_i, \theta_i, d_p, \sigma_p, n_p$

(b) SDPH

Fig. 1 Characteristics of smoothed particle hydrodynamics (SPH) particles in smoothed discrete particle hydrodynamics (SDPH) and traditional SPH

$$\langle f(\boldsymbol{r}_i) \rangle = \Sigma_{j=1}^{N} \frac{m_j}{\rho_j} f(\boldsymbol{r}_i) W_{ij} \tag{8}$$

$$\langle \nabla \cdot f(\boldsymbol{r}_i) \rangle = \Sigma_{j=1}^{N} \frac{m_j}{\rho_j} f(\boldsymbol{r}_i) \cdot \nabla W_{ij} \tag{9}$$

where m, ρ, and r denote the mass, effective density, and spatial position vector, respectively. $W_{ij} = W(r_i - r_j, h)$ is either a smoothing or kernel function. In this study, the cubic spline kernel function was used. Here, h is the smoothing length, the value of h is 1.3 times the initial particle spacing in this study.

Conservation equations for the discrete grain phase

The mass and momentum conservation equations for the discrete phase p are, respectively, as follows:

$$\frac{\partial}{\partial t}(\xi_f \rho_f) + \nabla \cdot (\xi_f \rho_f \boldsymbol{v}_f) = 0, \tag{10}$$

$$\frac{\partial}{\partial t}(\xi_f \rho_f \boldsymbol{v}_f) + \nabla \cdot (\xi_f \rho_f \boldsymbol{v}_f \boldsymbol{v}_f) = -\xi_f \nabla P_f + \nabla \cdot \boldsymbol{\tau}_f + \boldsymbol{R}_{fp} + \xi_f \rho_f \boldsymbol{g} + \boldsymbol{R}_{pf}. \tag{11}$$

where ξ_p, ρ_p, and $\boldsymbol{v}_p$ are the volume fraction, density, and velocity of the solid grain, respectively; P_p is the pressure of continuous phase; $\boldsymbol{\tau}_p$ is the discrete phase viscous stress tensor; and $\boldsymbol{R}_{pf}$ is the interaction force between the solid and liquid phases. The role of the drag force was mainly focused on, and the lift and virtual forces were not considered.

Rheological and constitutive laws

The granular flow materials are described as incompressible fluids. An elastic-viscoplastic constitutive model is used for the contact model of the grain–grain interactions. The hydrostatic pressure P is calculated directly from the granular constitutive equation using the standard definition of the mean stress, expressed as.

$$P = -\frac{1}{3}(\sigma^x + \sigma^y + \sigma^z), \tag{12}$$

where σ^x, σ^y, and σ^z are the components of the stress tensor in the x, y, and z directions, respectively. When a grain is in a quasi-static state, the grain as a whole experiences mainly elastic deformation. At elastic stage, the stress–strain relationship can be calculated according to the linear elastic model (Hooke's law):

$$\dot{\boldsymbol{\sigma}} = 2G\dot{\boldsymbol{e}} + K\dot{\varepsilon}\boldsymbol{\delta}, \tag{13}$$

where $\dot{\boldsymbol{\sigma}}$ is the incremental stress component tensor, G is the shear modulus ($G = \frac{E}{[2(1+\upsilon)]}$), K is the elastic bulk modulus ($K = \frac{E}{[3(1-2\upsilon)]}$), E is the elastic modulus (i.e., Young's modulus), υ is Poisson's ratio, and $\dot{\boldsymbol{e}}$ is the partial shear strain rate tensor ($\dot{\boldsymbol{e}} = \dot{\varepsilon} - \frac{\dot{\varepsilon}\boldsymbol{\delta}}{3}$). The strain rate tensor is defined as $\dot{\varepsilon} = \frac{1}{2}(\nabla \cdot \boldsymbol{v} + \nabla \cdot \boldsymbol{v}^T)$. This theory applies concepts in Drucker-Prager yield criterion. When the material yields, the constitutive law adopts the viscoplastic law.

At viscoplastic stage, numerous scholars have attempted to establish a viscoplastic continuum theory for dense granular media. At viscoplastic stage, the internal stress tensor can be given by the following relationship:

$$\boldsymbol{\sigma} = -P\boldsymbol{\delta} + \boldsymbol{\tau}, \tag{14}$$

$\boldsymbol{\tau}$ is the deviatoric stress component, defined as follows:

$$\boldsymbol{\tau} = \frac{\mu(I)P}{|\dot{\varepsilon}|}\dot{\varepsilon}, \tag{15}$$

where $|\dot{\varepsilon}|$ is the second invariant, $\dot{\varepsilon}$ is the strain rate tensor, which varies with the friction or viscosity coefficient of pseudo-fluid grains $\mu(I)$, and I is the inertia constant. This implies that there is a monotonic dependence of the volume fraction on the inertia constant. $\mu(I)$ is defined as.

$$\mu(I) = \mu_P + \frac{(\mu_2 - \mu_P)}{\left(\frac{I_0}{I} + 1\right)}, \tag{16}$$

where tests and numerical simulations have shown that in the $\mu(I)$ formula, the minimum value μ_P for a very low inertia constant I (quasi-static) gradually increases to a finite value μ_2 with increasing I (Jop et al. 2006). I_0 is a constant, and the parameters in the formula depend on the material properties. For example, the typical values are $\mu_s = \tan(21°)$, $\mu_2 = \tan(33°)$, and $I_0 = 0.28$ (MiDi 2004). I is defined as follows:

$$I = \frac{|\dot{\varepsilon}|d}{\left(\frac{P}{\rho_P}\right)^{0.5}}. \tag{17}$$

where the inertia constant expresses the ratio between the inertial time scale $\left(d_P^2 \rho_P/P\right)^{0.5}$ and the macroscopic deformation time scale $(1/|\dot{\varepsilon}|)$.

Solid–fluid two-phase coupling

Numerous studies have shown that the coupling algorithm between the grain and fluid in two-phase flow is very important (Iverson and Denlinger 2001; Pudasaini 2012; Pitman and Le 2005; Chen et al. 2017; Pastor et al. 2021; Tayyebi et al. 2022). The interphase forces play a key role in the coupling between the continuous fluid phase and the discrete solid phase. The interactions between components of one phase are also driven by the drag force of the other phase. Therefore, the grain phase data interacts with the continuous phase data in the process of calculating the internal stress, and the exchanged data includes the drag force and pressure. For both SPH and SDPH, the adjacent particle information is obtained using the proximity particle search method, so that the adjacent particle updates the main particle and the virtual particle information of the other phase. The simulation of the drag force requires the background particle bearing at the same position, and the interpolation obtains the velocity value of the other phase at this position, thereby allowing the drag force to be obtained. The time step of the coupling method is determined by the minimum time step of the SPH and SDPH methods. The simulation flowchart is shown in Fig. 2.

A review of the existing constitutive relations for the interaction forces was presented by Johnson (1990). The drag force of the fluid plays an important role in mixed fluids (Fig. 3a), and the lift and additional forces on the grains are negligible (Pudasaini and Hutter 2007; Si et al. 2018; Gao, et al. 2022). A drag law describes the interaction
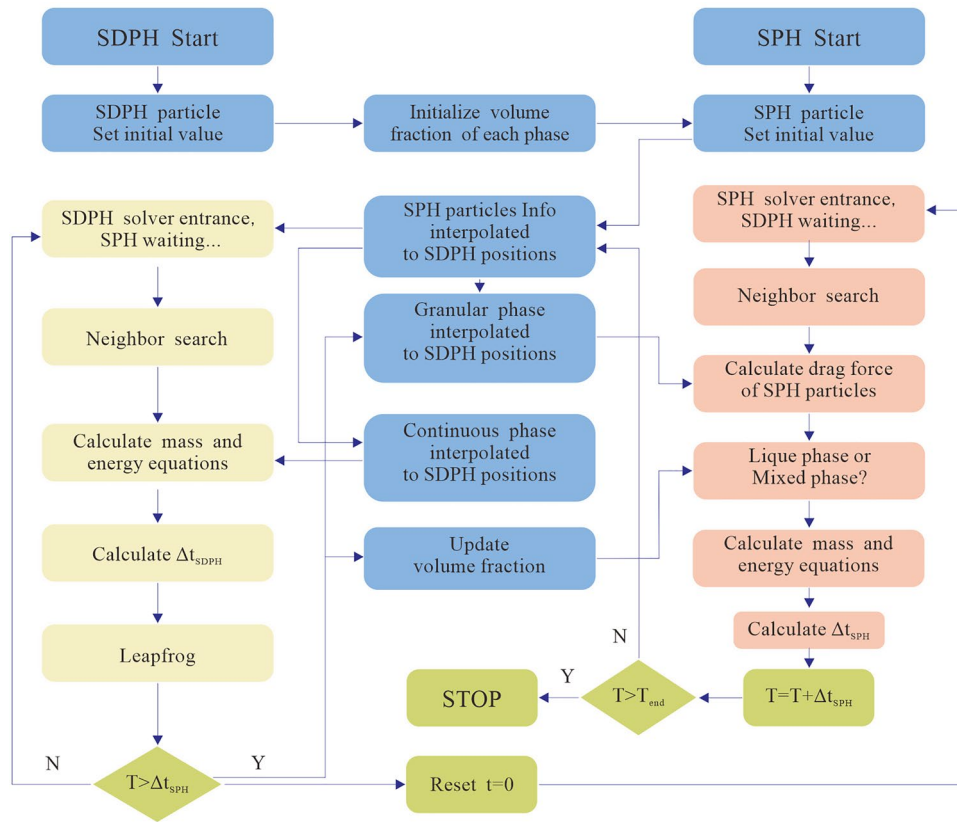
**Fig. 2** Schematic diagram of the SPH-SDPH coupling algorithm

between the interstitial fluid and the grains. The method proposed by Gidaspow was used, where the Ergun equation was used for the simulation of the dense phase and the Wen-Yu equation was used for the simulation of the dilute phase (Gidaspow 1994; Ergun 1952; Wen and Yu 1966):

$$\beta = \begin{cases} \beta_{Ergun} = 150 \frac{\xi_P^2 \mu_f}{\xi_f d_P^2} + 1.75 \frac{\xi_P \rho_f}{d_P} \left| v_f - v_p \right|, \xi_f < 0.8 \\ \beta_{Wen} - Yu = \frac{3}{4} C_D \frac{\xi_P \xi_f \rho_f}{d_P} \left| v_f - v_p \right| \xi_P^{-2.65}, \xi_f \geq 0.8 \end{cases} . \quad (18)$$

where β is the momentum transfer coefficient between the fluid and solid; C_D is the traction coefficient; ξ_P and ξ_f volume fractions of the solid and the fluid, respectively; μ_f is fluid viscosity coefficient; d_P is the diameter of the discrete particles; ρ_f is the fluid density; v_f and v_P represent the velocity of the fluid and solid, respectively.

The drag force coefficient C_D is.

$$C_D \begin{cases} \frac{24}{\xi_f Re_P} \left[1 + 0.15 \left(\xi_f Re_P \right)^{0.687} \right], & Re_P < 1000 \\ 0.44 & Re_P < 1000 \end{cases} . \quad (19)$$

(a)   (b)
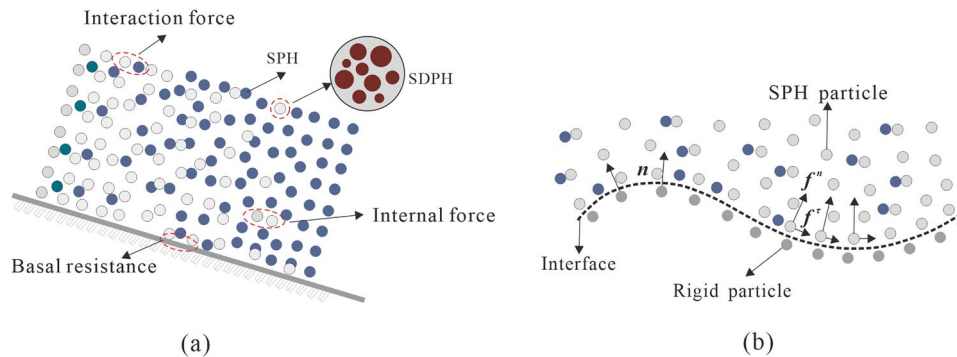
Fig. 3 Schematic diagram of the two-phase interactions: **a** interactions between fluid and solid grains and **b** Interactions between sliding main body and boundaries

The relative Reynolds number Re_P is defined as.

$$Re_P = \frac{\rho_f d_P \left| v_f - v_p \right|}{\mu_f}.$$ (20)

In order to eliminate the discontinuity between the two equations, a relaxation factor was introduced to smooth the momentum exchange coefficient in the transition zone:

$$\varphi_{fP} = \frac{arctan\left[150 \times 1.75\left(0.2 - \xi_P\right)\right]}{\pi} + 0.5.$$ (21)

Therefore, the momentum exchange coefficient β can be expressed as.

$$\beta = \left(1 - \varphi_{fP}\right)\beta_{Ergun} + \varphi_{fP}\beta_{Wen-Yu}.$$ (22)

Thus, the drag force R_{pf} per unit mass of the grain can be calculated as follows:

$$R_{pf} = \frac{\beta_{fP}\left(v_f - v_p\right)}{\xi_P \rho_P}.$$ (23)

where v_f and v_p are the velocities of the solid and the fluid, respectively.

Boundary conditions

In response to the full three-dimension numerical algorithm boundary forces are particularly critical and affect the particle failure. The forces between the grains and the boundary were decomposed into a normal force f^n and a tangential force f^τ (Fig. 3b). The boundary normal force is applied Penalty function formula (Eq. 24), which the repulsive force is directly applied on the boundary particles. The penalty parameter was modified to make it proportional to the distance and velocity between the particles and the boundary (Li and Liu 2002). The boundary tangential force was selected according to the material properties of the sliding body, and different resistance models were used for the fluid and the solid.

Normal force
For the normal force, the contact condition was defined by the penalty function equation:

$$f^n \begin{cases} -\omega 2h_i \sum_{j\in B}\left(\frac{1}{|r_{ij}|}(\mathbf{v}_i - \mathbf{v}_j^B)\cdot \boldsymbol{n}_j W_{ij}A_j\boldsymbol{n}_j\right) & v_i \cdot n_j < 0 \\ 0 & v_i \cdot n_j \geq 0 \end{cases},$$ (24)

where ω is the penalty parameter, r_{ij} is the radial vector between grain i and grain j, v_i is the velocity vector of grain i, v_j^B is the velocity vector of boundary grain j, n_j is the normal vector of boundary grain j, W_{ij} is the kernel function between grain i and grain j, and A_j is the area of boundary grain j.

Tangential force
The frictional model of the solid is as follows:

$$f^\tau = \sigma\left(1 - r_u\right)tan\phi,$$ (25)

where σ is only a function of the total normal stress at the bottom, r_u is the pore pressure coefficient, and Φ is the friction angle. The value of the friction coefficient can be calculated from $tan\Phi$.

The laminar model of the fluid is as follows:

$$f^\tau = \frac{3vu}{H},$$ (26)

where μ is the dynamic viscosity coefficient, v is the velocity of the fluid, and H is the fluid depth.

Numerical modeling verification
The LPF³ᴰ can realize the high-efficiency and high-precision solution of complex dynamic problems of long-runout flow-like landslide with solid–liquid mixed two phases. There are mainly several aspects merit as follows: (i) solves the problem of calculating discrete particles in continuum medium, improves the simulation accuracy by comparing the discrete element method; (ii) can solve efficiently to the dynamics process of three-dimensional complex solid–fluid coupling problems under the same numerical algorithm framework; (iii) compared with the selection of empirical parameters based on depth integration method, the selection of material numerical parameters can be more consistent with mechanical parameters of the realistic material; (iv) some progress has been made in geometric modeling, dynamic boundary mechanics application, and maximum number of particles that is 600,000. Comparison analyses of small-scale flume experiments and realistic-scale landslide cases and different numerical methods were performed to show that this numerical modeling is capable of simulating mixed two-phase flow.

Flume experiment of two-phase flow

In this paper, small-scale flume experiments were carried out on solid–fluid mixed material. In order to ensure that the fluid content in the two-phase flow was consistent with that in actual conditions and to compare the effect of the fluid on the solid grains for different volume fractions, experiments were carried out under three conditions: I. dry grains only, II. dry grains mixed with clear water with a 30% volume fraction, and III. dry grains mixed with clear water with a 70% volume fraction. The experiment purpose is to check the numerical model and algorithm parameters. (i) In flume experiment. The flume is made up of chute (length × width × height = 300 cm × 50 cm × 50 cm), slide hopper (length × width × height = 50 cm × 50 cm × 50 cm), and bottom plate (length × width = 600 cm × 240 cm) (Fig. 4a). The angle of inclination is uniformly selected as 20°. The solid material in the flume experiment was limestone gravel grains and selected 2–10 mm particle size. The fluid material adopted clear water. Both solid and fluid materials are fully mixed in the hopper. (ii) In numerical simulation. The physical and mechanical parameters of the material and SPH algorithm parameters in experimental are shown in Table 1. The motion process and deposition shape of the fluid and solids were back analysis using the LPF³ᴰ, and the imaginary speed of sound, artificial heat quantity (α/β/η), artificial viscosity (α/β/η), etc., for algorithm parameters were confirmed.
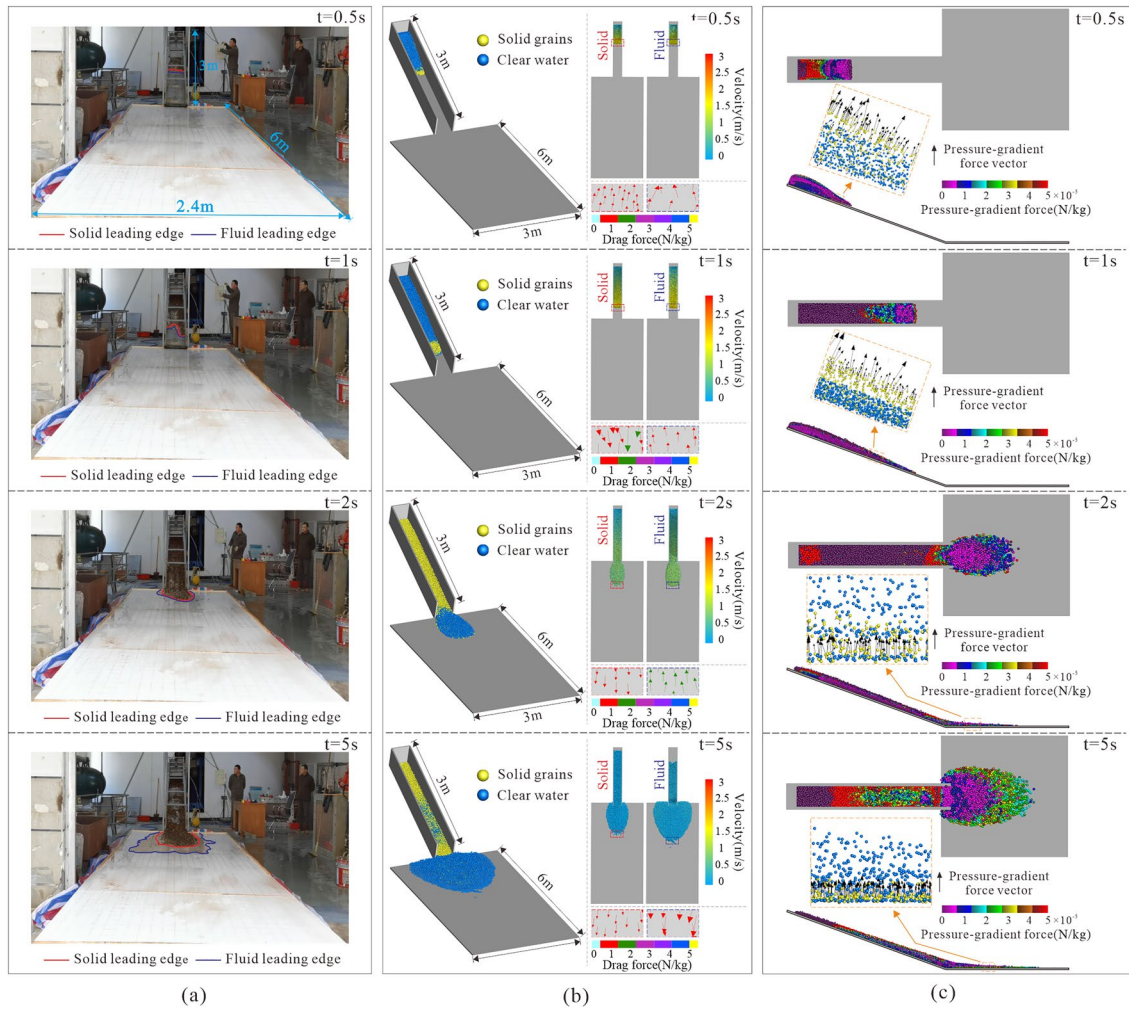
Fig. 4 Flume experiment and numerical simulation results under condition II. **a** Actual experimental results, which blue solid lines represent the fluid deposition range and the red solid lines represent the solid particle packing range. **b** The velocity distribution plot and the drag force vector. **c** Water the pressure gradient force on the solid grain distribution plot and vector

In the working condition I of only dry grains, the mass of the grains was 100 kg. The friction coefficient of the boundary condition was particularly critical to ensure the simulation results were consistent with the test. Through multiple trial and error simulations, the friction coefficient of 0.8 was found to be the most appropriate for dry grains. In the simulation of working conditions II and III, the friction coefficient between the grains and the boundary layer was also selected as 0.8. In the analysis of the latter two conditions, the drag force and water pressure were important in the coupled simulation.

In working condition II of grains mixed with 30% volume fraction of water, dry grains were mixed with 30% water and slid down along the flume. The mass of the grains was 100 kg, and the mass of the water was 23.1 kg. Four time stages, 0.5, 1, 2, and 5 s, were chosen to represent the entire motion process of the simulated mixed two-phase. From the deposition results, it can be seen that the coupled grains with water moved and deposited on the bottom plate, and the travel distance was about 5.2 m (Fig. 4a). Figure 4b shows the simulation results in the LPF³ᴰ software. At 0.5 s, the

mixture slid out of the starting area and reached the bottom plate at 2 s. The simulation results were able to reconstruct the motion process under condition II. The velocity difference between the fluid and the solid grains was a key influencing factor of the drag force. Figure 4b shows the velocity contour map of the fluid-grain phase at the four time points. After sliding main body releasing, the solid grains slide down along the flume. Although the solid velocity is higher than fluid at the leading edge in the initial stage, the fluid velocity exceeds the solid velocity in the deceleration stage. And the fluid dragged solid grains to continue in motion due to the solid–liquid velocity difference. In this paper, the fluid pressure gradient force was used to reflect the fluid pressure distribution acting on the solid. The fluid pressure gradient force on the solid grains is normal direction of the motion path. From the top view of the pressure gradient force on the grains, it can be seen that the value of the pressure gradient force is larger at the sliding source area of hopper, the exit terrain turning position of the chute, and the leading edge of the sliding main body (Fig. 4c). From the side view of the pressure gradient force, the water pressure gradient

Table 1 LPF3D simulation parameters of two-phase flow flume experimental simulation

Material parameters

Working condition	Grain phase				Basal pore pressure coefficient		Fluid phase (clear water)		
	Mass (kg)	Density (kg/m³)	Grain diameter (m)	Friction coefficient	Flume	Bottom plate	Density (kg/m³)	Fluid volume fraction (%)	Dynamic viscosity (Pa·s)
I	100	2600	0.02	0.8	—	—	—	—	—
II	100	2600	0.02	0.8	0.5	0.7	1000	30	0.001
III	100	2600	0.02	0.8	0.55	0.8	1000	70	0.001

SPH algorithm parameters

Number of solid particles	Number of fluid particles	Time step	Imaginary speed of sound	Artificial heat quantity ($\alpha/\beta/\eta$)	Artificial viscosity ($\alpha/\beta/\eta$)
7980	12,696	0.0001	10	0.01/0.02/0.01	0.01/0.02/0.01

force increases the uplift pressure of solid grains. The fluid pressure gradient force due to the up and down surface pressure difference of the solid grain is greater when solid particles are located on the fluid surface.

In working condition III of grains mixed with 70% volume fraction of water and slide down the same flume, the mass of the grains was 100 kg and the mass of the water was 53.8 kg. Also four time points, 0.5, 1, 2, and 5 s, were chosen to represent the entire motion process of the simulated debris flow. From the deposition results, it can be seen that the grains coupled with water moved and deposited on the bottom plate, and the deposition at the exit of the flume was dense, while that in the front was relatively loose. The travel distance reached about 8.2 m (Fig. 5a). Figure 5b shows the simulation results from the LPF^{3D} method. The mixture slid out of the starting area at 0.5 s and reached the bottom plate at 1 s. The simulation results were able to reconstruct the motion process under condition III. The velocity difference between the fluid and the solid grains is a key influencing factor of the drag force. Figure 5b shows the velocity contour map of the fluid–solid phase at the four time points. Compared to working condition II, when the fluid volume fraction is larger, the leading edge velocity of the fluid is larger than the solid in the initial stage, and the fluid dragged solid grains throughout the motion process. The initial volume fraction of the fluid is very important for its influence on the drag force and deposition shape feature. The fluid pressure gradient force distribution is consistent with working condition II.

Based on the velocity curves of the grains, the larger the fluid volume fraction was, the faster the grain velocity was. Moreover, the velocity variation of the grains was basically the same as that of the fluid. The results showed that the travel time and movement velocity of the mixed sliding body changed significantly compared with those of the pure dry grains, indicating a significant dragging effect of the fluid on the solid grains (Fig. 6a). When the fluid volume fraction is low, the leading edge velocity of the fluid is smaller than the solid that appears in the initial stage. But the overall average velocity of the fluid is larger than the solid (Fig. 6b). The average velocity of fluid is higher than solid. The average velocity of the solid particles and the fluid are shown in Fig. 6b. The average velocity of fluid is higher than solid. The solid mass is consistent, the larger the fluid volume fraction, the larger the solid velocity. Figure 6c shows the larger the fluid volume fraction was, the stronger the drag force acting on the solid grains. Moreover, due to the presence of fluid, the friction energy consumption between the solid grains decreased. As a result, the grain motion became more consistent with the fluid motion, and the drag force led to increased grain motion. The full three-dimensional accumulation results are relatively better restored to the actual flume experimental results except for some local differences (Fig. 6d).

Landslide case study-Sanxicun landslide

To verify the effectiveness of LPF^{3D} for realistic landslide scale simulation, the Sanxicun landslide was selected for simulation validation. On July 10, 2013, Sanxicun long runout flow-like landslide, Dujiangyan City, Sichuan, resulted in 166 deaths. The landslide involved displaced material from the source area of 1.9 million m³ and about 0.30 million m³ in front of the sliding main body to form a debris flow. The runout of debris flow had
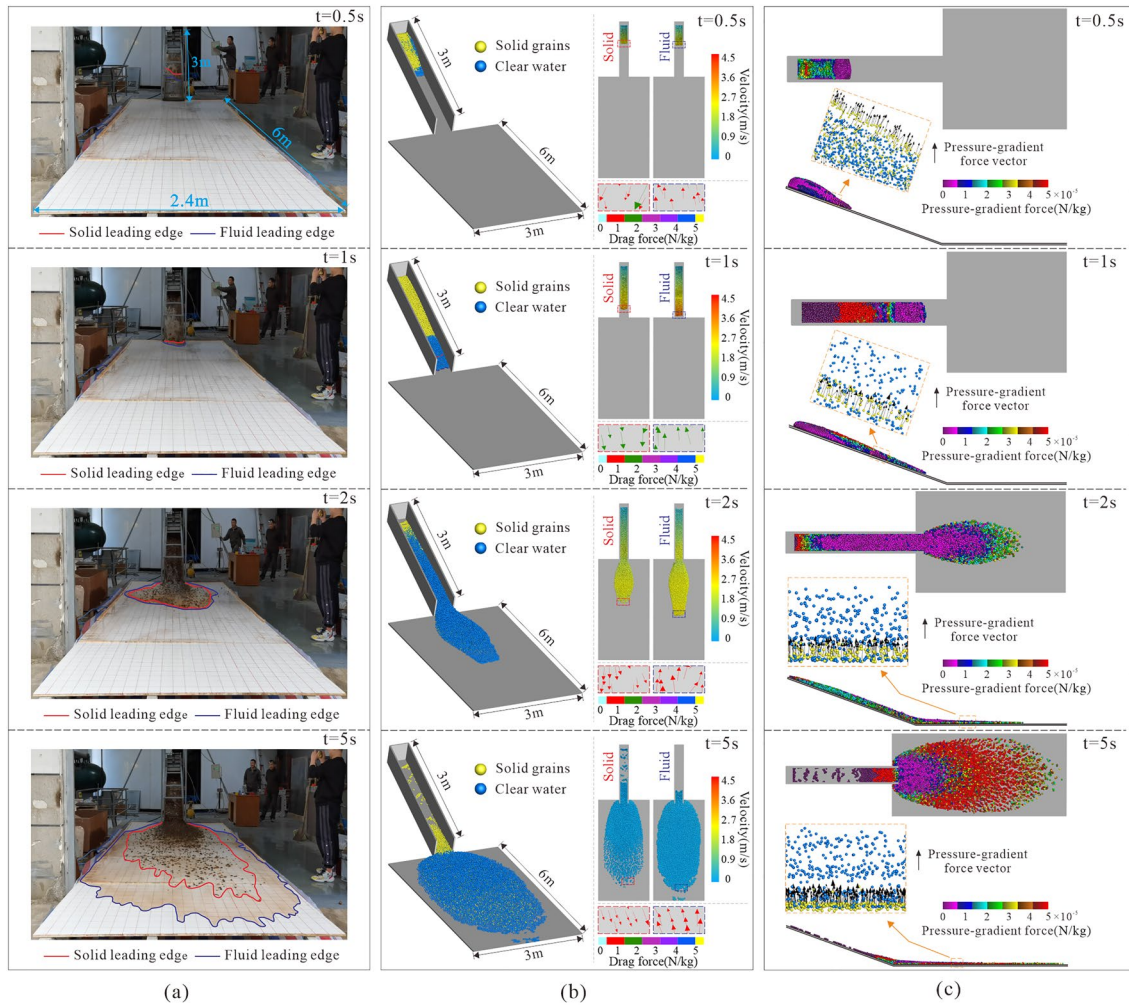
Fig. 5 Flume experiment and numerical simulation results under condition III. **a** Actual experimental results, which blue solid lines represent the fluid packing range and the red solid lines represent the solid particle packing range. **b** The velocity distribution plot and the drag force vector. **c** The water pressure gradient force on the solid grain distribution plot and vector

a horizontal extent of 1200 m and a vertical extent of 400 m, and covered an area of 0.2 km² (Yin et al. 2016; Gao et al. 2017). The sliding main body is mostly bedrock, including sandstone and mudstone, and mixed with the ground surface runoff under heavy participates, then translated into debris flow, resulting in long runout disasters (Fig. 7).

To ensure more finely restore the local terrain accuracy in three dimensions, a high precision terrain of 1:2000 was used in Sanxicun landslide. The physical and mechanical parameters of the sliding body were based on actual measurements. The solid grains parameters were used by sandstone and mudstone grains, and the fluid was used by slurry. The influence of the fluid on the landslide was mainly through the pore water pressure and interphase interaction forces. For the purpose of comparison, four working conditions were analyzed: I. Dry grain numerical test and II. basal lubrication. When water is mixed in the sliding main body, the basal boundary has a certain lubrication. The tangential friction resistance will be reduced. This working condition II is used as the comparison sample for analyzing boundary

tangential resistance. The drag force is also key to the landslide mobility in different volume fractures of fluid in three dimensions. The tangential friction coefficient of working conditions III and IV is consistent with the working condition II, and the initial fluid volume fractions were set to 30% and 60%, respectively. The sum of the fluid volume fraction and the grain volume fraction was equal to 100% in the two-phase coupling state. In the numerical simulation, the basal friction coefficient was critical to the traveling distance of the landslide. The volume of the landslide body is also a key factor in determining to friction coefficient. Small-scale rockslides have a coefficient of friction between 0.6 and 0.7, while large thick-layered rockslides can be less than 0.3 (Yamada et al. 2018). The volume of the sliding main body is 0.30 million m³, so the friction coefficient is set to 0.6. The pore pressure coefficient of r_u is 0.4 in Eq. (25). The movement distance, accumulation range, and accumulation thickness of the landslide are taken according to field site observation. The algorithm parameters are consistent with the flume experiment. The specific parameters are shown in Table 2.
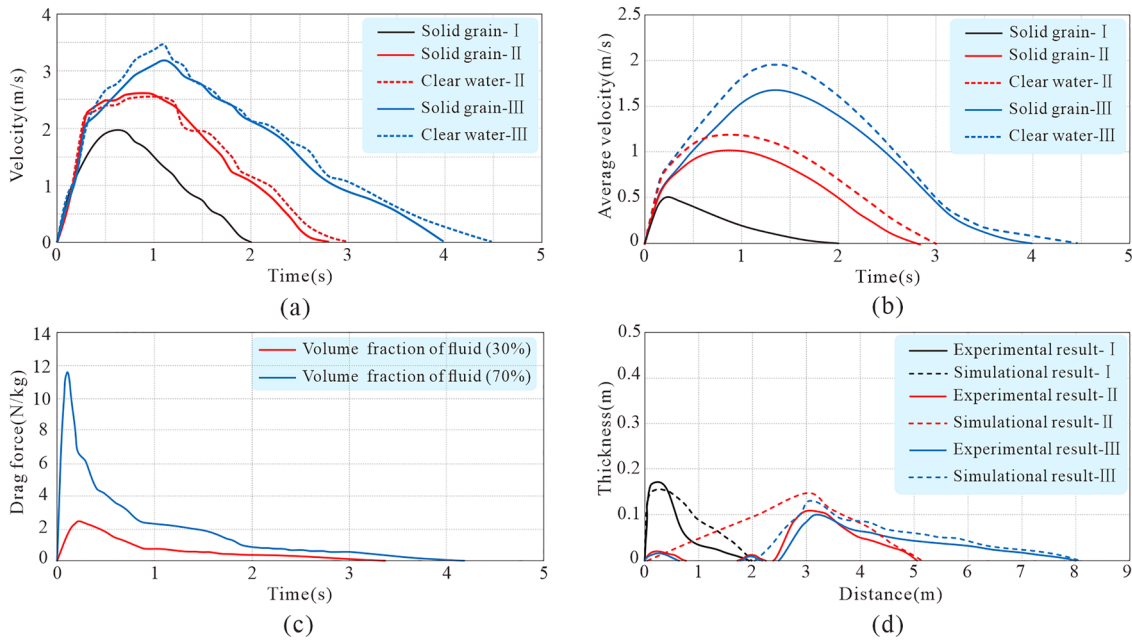
Fig. 6 Flume experiments. **a** Velocity variations at the leading edges of different phases in the sliding main body. **b** Average velocity of all particles at different moments of the sliding main body. **c** Average drag force per unit mass of all particles at different moments under different volume fractions of the fluid. **d** Comparison of solid grain final accumulation profile along the center line

The results of the four conditions, which are shown in Fig. 8, are summarized as follows: Working condition I: It is like a rock collapse. The travel distance under the dry grains was the smallest. Working condition II: When low friction lubrication on the substrate boundary was considered, the travel distance of the landslide increased, but it still did not cause the whole sliding mass to slide down. Working condition III: When the fluid volume fraction was 30%, due to basal lubrication and the interphase forces between the fluid and grains, the traveling distance of the sliding main body increased significantly, but it was quite different from that of an actual landslide. Working condition IV: When the fluid volume fraction was 60%, the result was almost consistent with the realistic landslide. When the influences of the sliding main body are dominated by bedrock with a large porosity and abundant ground surface runoff, the fluid volume fraction and interphase forces should be considered to explore the mobility of long runout landslides. Figures 9, 10, and 11 show the numerical simulation results of Sanxicun landslide in working conditions IV.

After the Sanxicun landslide was activated, the rock mass quickly collapsed and fragmented to form a debris avalanche, and solid grains mixed with the abundant ground surface runoff generated by the heavy rainfall formed a debris flow. After hitting the mountain on the right, the debris flow turned from northeast to northwest, damaging and burying farm buildings along the way, and then it finally stopped. The simulation results showed that the Sanxicun landslide lasted about 80 s (Fig. 9). After the landslide started moving at a high elevation, the speed increased rapidly after passing through the steep terrain, and the speed reached 25 m/s at 10 s. Afterward, due to the narrowness of the channel, the fluid velocity further increased, resulting in an increase in the velocity of the solid grains. Around 20 s, the landslide body hit the mountain

on the right, and the solid velocity increased to a peak value of 31 m/s. Then, due to the terrain of the channel, the rock and soil mass collided with the mountain, and the main sliding direction changed by 350°. At $T = 40$ s, most of the rock and soil mass reached the channel deflection area, and the velocity dropped to 12 m/s. As the direction of the rock and soil mass was changed, the solid–fluid mixture traveled to a relatively broad and flat terrain, and the speed gradually decreased. At about 80 s, the landslide stopped.

The distribution of the drag force on solid grains is shown in Fig. 10. The dark blue grains represent fluids, and the rest are solid grains. The color gradients represent the magnitude of the drag force per unit mass of solid grains. In the landslide motion process, when the fluids and the solid grains mixed and moved together, the solid grains were significantly affected by the drag force of the fluid. The magnitude of the drag force was mainly determined by the velocity differences between the fluid and solid phases. The arrows are the drag force vectors of the solid grains. Figure 11 shows a contour map of the deposition thickness during the Sanxicun landslide. The red line represents the actual range of the landslide, and the red, yellow, and blue colors reflect the changes in the deposition thickness. During the landslide motion process, the debris flow moved in the northeast direction and then changed to the northwest direction after passing through the channel deflection area. The area with a large deposition thickness was located in the middle of the landslide. When the grains stopped moving, the front edge of the landslide deposited in the channel. The maximum travel distance of the landslide was 1200 m, and the maximum deposition thickness reached about 12 m. The deposition result was consistent with the actual field observations.

The velocity difference between the slurry flow and the solid grains is a key influencing factor of the drag force. In order to further understand the influence of drag development on the
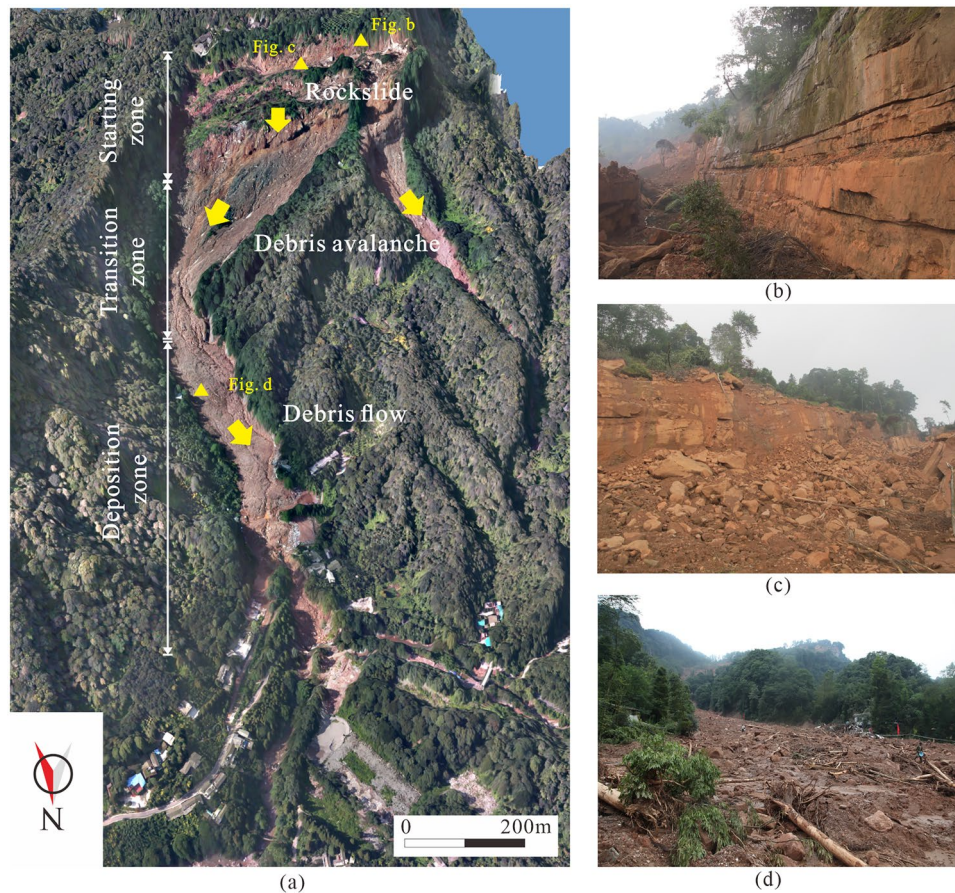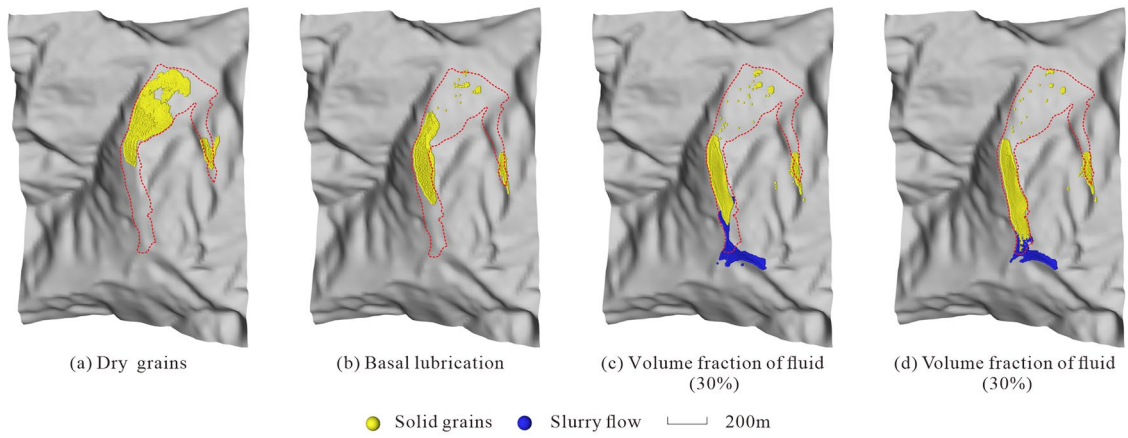
Fig. 7 Aerial view and photograph of the 2013 Sanxicun long runout landslide in Sichuan, China. **a** Aerial view. **b** Complete rock mass at the trailing edge of the landslide. **c** Disintegration of the debris remaining in the starting area after the trailing edge of the landslide. **d** Deposition from the debris flow

movement of solid grains in the Sanxicun landslide, two velocity curves were selected for comparison. Figure 12a shows the leading edge velocity of the sliding main body under the four conditions. In the initial sliding and acceleration stages, the velocities of the solid grains and slurry flow were similar. Due to the larger fluid volume fraction in condition IV, the friction between solid grains and the slurry flow was reduced, and there was less energy loss. Thus, the velocities of the solid grains in condition

IV were greater than those in condition III. As the landslide collided with the mountain on the right, the velocity fluctuated significantly. The velocity of the slurry flow was always greater than that of the solid grains. Figure 12b shows the average velocity curves for all solid grains and fluid under four working conditions. The maximum average velocity of the fluid is 31 m/s and the maximum average velocity of the solid grains is 22 m/s. The presence of fluid in sliding main body increased velocity

Table 2 LPF3D numerical simulation parameters of Sanxicun landslide

Working condition	Grain phase				Fluid phase (slurry)		
	Density (kg/m³)	Grain diameter (m)	Friction coefficient	Basal pore pressure coefficient	Density (kg/m³)	Viscosity coefficient (Pa·s)	Volume fraction of fluid
I	2600	0.5	0.6	0	-	-	0
II	2600	0.5	0.6	0	-	-	0
III	2600	0.5	0.6	0.4	1300	0.2	30%
IV	2600	0.5	0.6	0.4	1300	0.2	60%

(a) Dry grains   (b) Basal lubrication   (c) Volume fraction of fluid (30%)   (d) Volume fraction of fluid (30%)

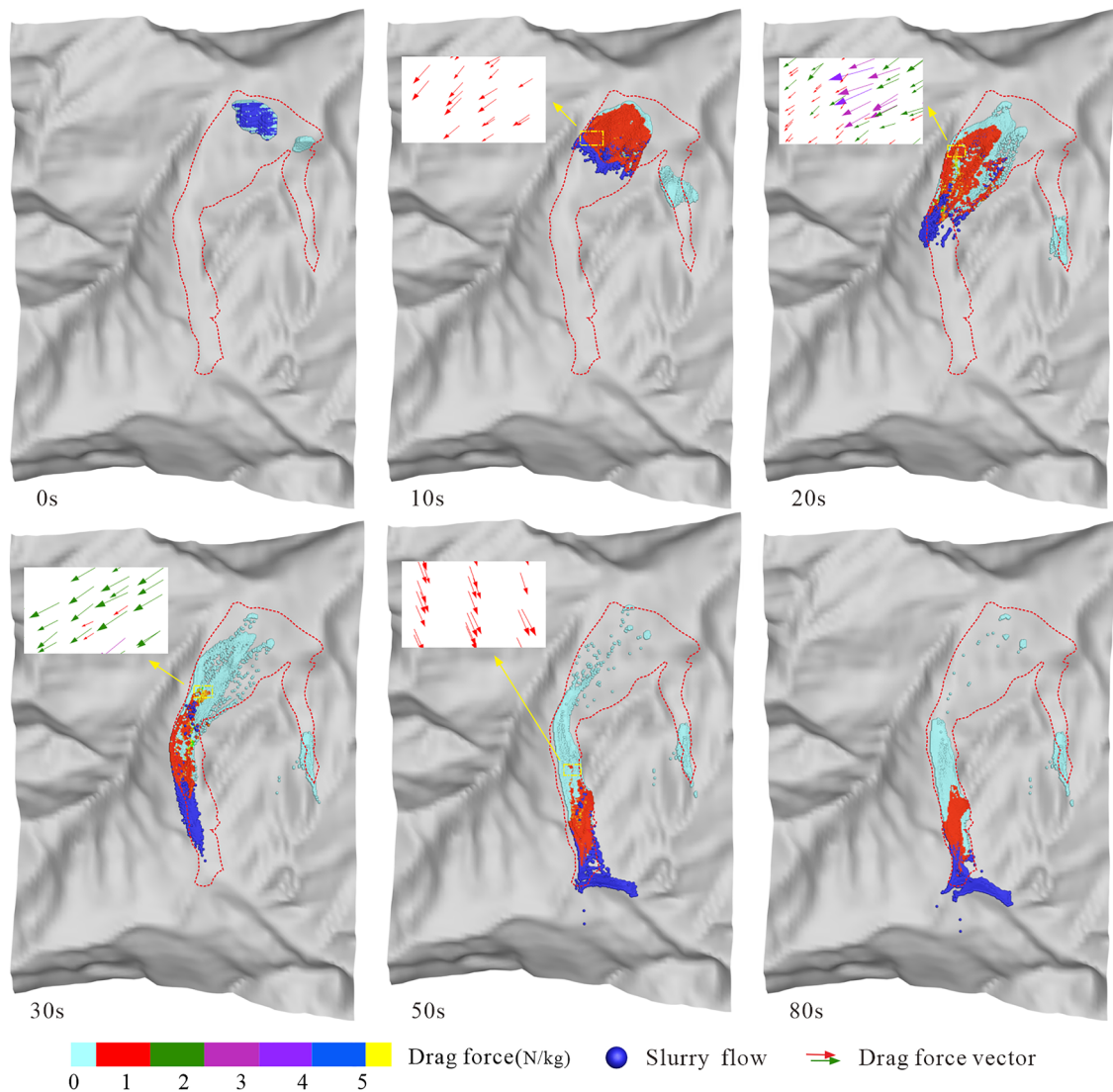⬤ Solid grains   ⬤ Slurry flow   ⊢⊣ 200m

Fig. 8 Comparison of numerical simulation results of the Sanxicun landslide under four working conditions

0s   10s   20s

30s   50s   80s

Velocity(m/s)   ⬤ Slurry flow
0   5   10   15   20   25   30   35   40   45
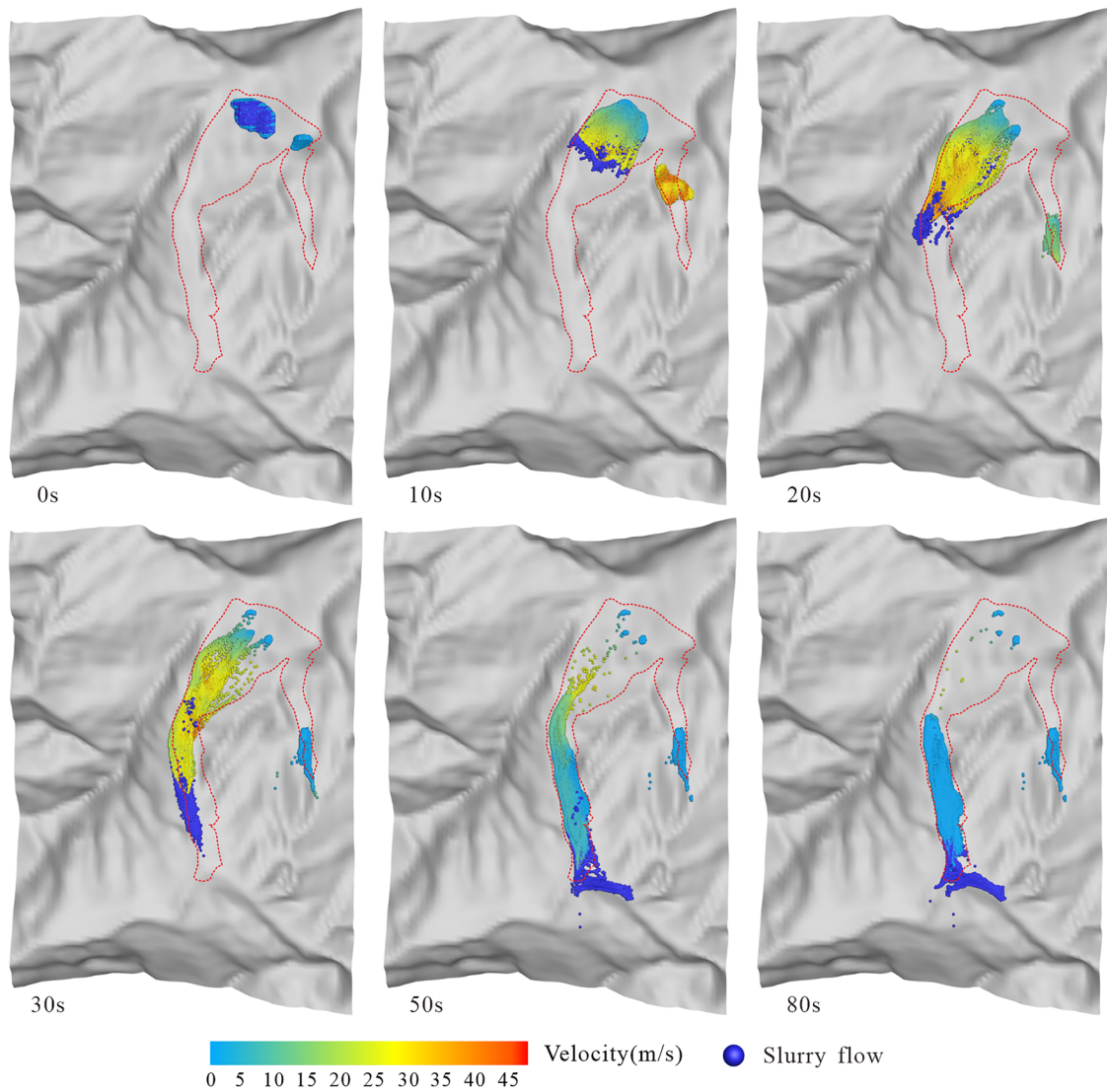
Fig. 9 LPF3D simulated velocity distribution of the Sanxicun landslide

Fig. 10 Fluid drag force distribution during motion process of the Sanxicun landslide

and mobility of the solid grains, due to the basal lubrication and fluid drag forces. Under the same physical and mechanical parameters, the larger the fluid volume fraction, the higher the average velocity of the solid grains. Fluid drag force plays a significant role in solid–liquid two-phase landslides.

Comparison and discussion of different numerical methods

It is important to compare different numerical methods with the same geometric model, same mechanical model, and same dynamics parameters. In the comparative analysis, three numerical methods are mainly used for comparison: DEM-FVM coupling method, DAN3D equivalent fluid method, and LPF^{3D} method. The applicability of LPF^{3D} is proved by comparing the numerical results with the realistic landslide accumulation results.

Model and parameter selection

The simulation case selects the Xianchi reservoir long runout flow-like landslide. At 22:00 pm on September 1, 2014, a catastrophic landslide occurred in the Yunyang area of Chongqing City, causing 508 persons evacuations and the burying or damage of 23 buildings (Fig. 13). From August 31 to September 2, 2014, a 50-year heavy rainstorm hit the Northeastern Chongqing area, China. Xianchi station in Yunyang County experienced the most concentrated rainfall, with a daily rainfall of 403.4 mm/day (Li et al. 2022). The landslide involved displaced material from the source area of 1.44 million m^3. The runout of debris flow had a horizontal extent of 1600 m and a vertical extent of 400 m, and covered an area of 0.142 km^2. The 1:2000 terrain and sliding main body geometry model were based on topography contour data, and the physical and mechanical parameters were based on previous research literature (Gao
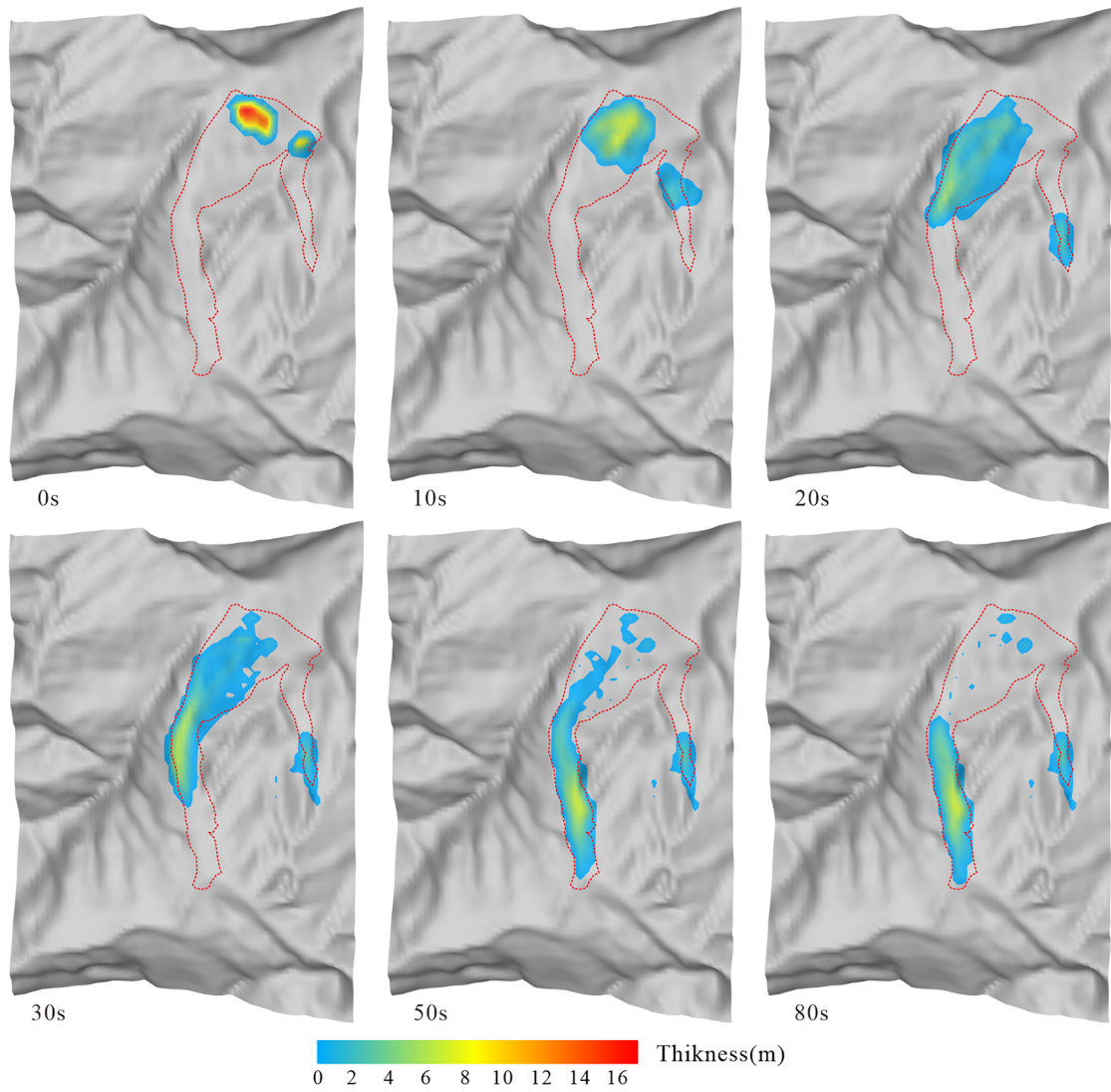
**Fig. 11** Deposition thickness distribution contours during motion process of the Sanxicun landslide

et al. 2022). The specific parameters are shown in Table 3. For the purpose of comparison, the physical model, mechanical model, and simulation parameters are all consistent, and three numerical simulation results were analyzed by EDEM-Fluent (DEM-FVM coupled method), LPF3D (SDPH-SPH method), and DAN3D (SPH equivalent fluid method of depth averaged).

(a) Leading edge velocity of the sliding main boding

(b) Average velocity of all particles
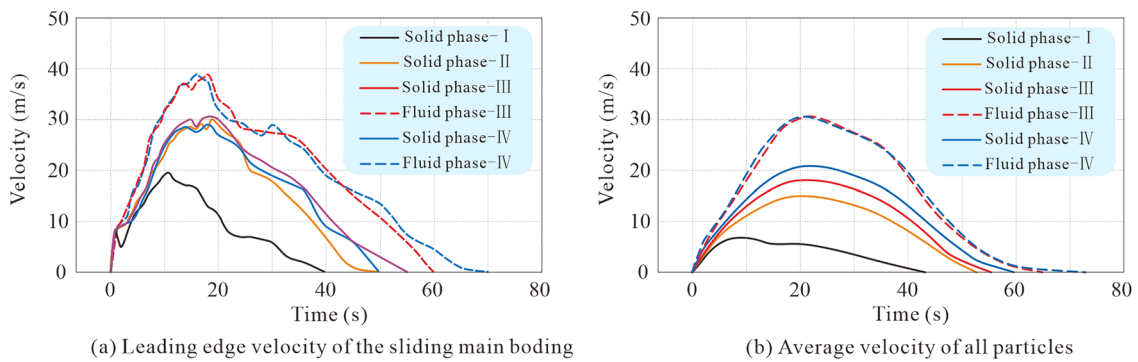
Fig. 12 Velocity curves of solid and fluid under four working conditions. **a** The leading edge velocity of the sliding main body. **b** The average velocity of all particles

(a) The Xianchi reservoir landslide

(b) Source area

(c) Propagation area

(d) Accumulation area
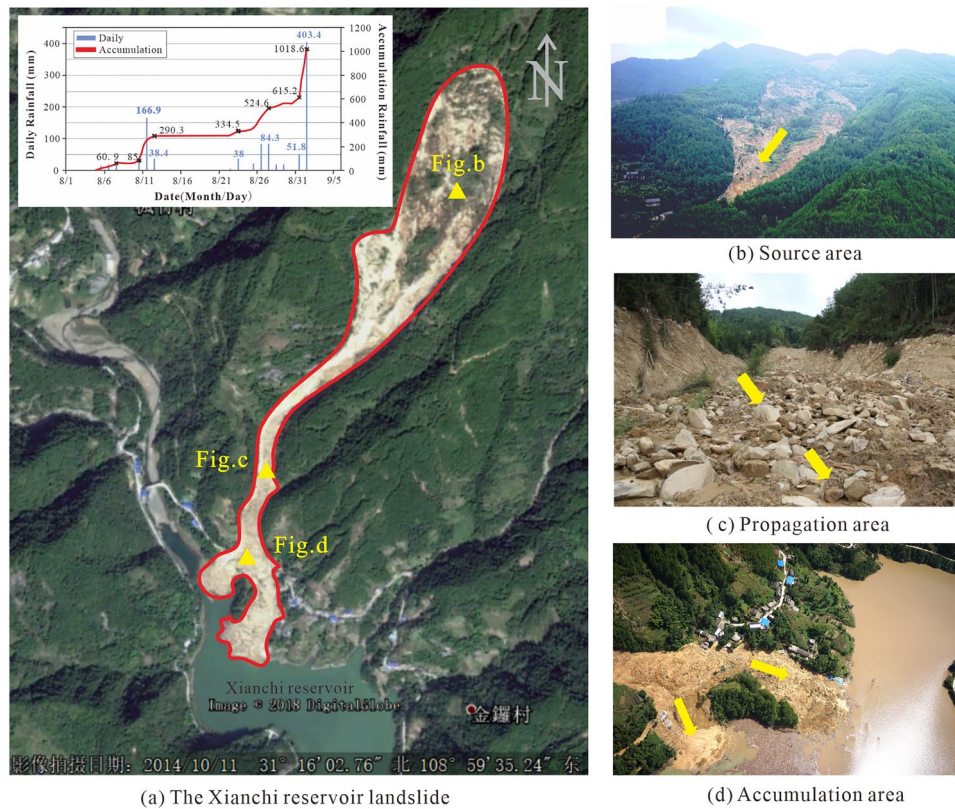
Fig. 13 Remote sensing diagram and photograph of the September 1, 2014, Xianchi reservoir landslide in Yunyang, Chongqing, China. This landslide belongs to long runout flow-like landslide with solid–liquid two-phase, and then developed into debris flow under heavy rainfall. The sliding main body was approximately 1.44 million m^3. This was equivalent to a fahrböschung angle of 14° and covered an area of 0.142 km^2

Comparison of numerical simulation results comparison with equivalent fluid numerical model (DAN3D)

In the comparative analysis of the same geometric model, same mechanical model, and same dynamics parameters, the DAN3D simulation software was used to compare different landslide types. The sliding main body was considered to be debris avalanche, and the friction model was selected for the basal resistance model. Then, the sliding main body was considered mud flow, and Newton laminar flow model was used as the basal resistance model. Under the same simulation parameters, the accumulation results for the above two cases were almost consistent with the LPF^{3D} results. Hence, the numerical simulation result respectively verified the reliability of LPF^{3D} for single-phase flow (Fig. 14). At the same time, this method is a full three-dimensional simulation, which has better advantages in reproducing the internal action and local motion detail of sliding main body. Detailed result data are shown in Table 4. Heavy rainfall plays a key role in the long runout motion process of two-phase flow-like landslide. The sliding main body hardly moves in the dry condition, but under the action of heavy rainfall, the fluid and solid particles are coupled to generate a long runout motion distance (Fig. 15a). Numerical simulation results of LPF^{3D} demonstrate the importance of interaction force between fluid and solid phases. Figure 15b shows that the fluid drag force acts on the solid along the direction of motion. In the acceleration stage of the landslide,
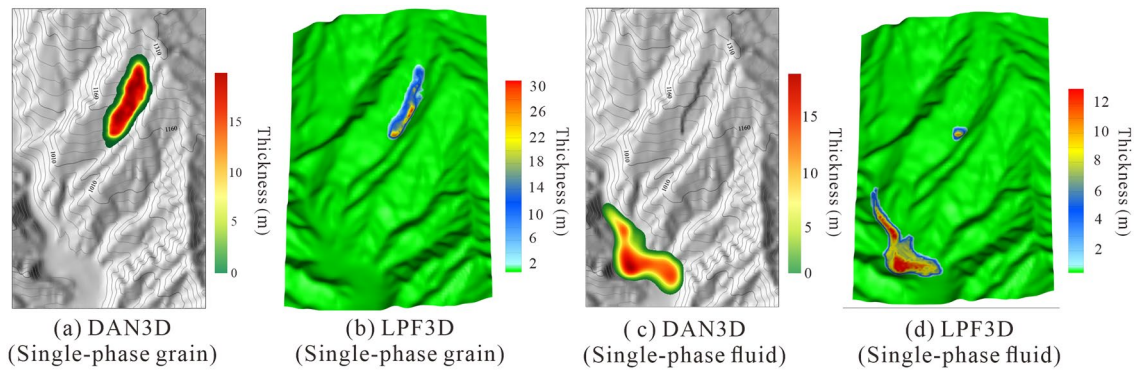
this effect is more significant. Figure 15c shows that the fluid pressure gradient force acts on the solid along the vertical direction of motion, and the value is correlated with the solid normal stress. This value is larger at certain positions, such as the turning point of the terrain, the leading edge of the sliding main body, and the solid large packing thickness position.

Comparison with mixed two-phase flow numerical model (DEM-FVM)

The coupled algorithm has more advantages for model and parameter selection than the single phase. The parameters for a single-phase solid grain or fluid are relatively easy to obtain. However, if the mixture of solid grain and fluid is equivalent to a single fluid, the selection of parameters is random and mostly depends on the experience of geologists. For example, in DAN3D simulation, the results of high coincidence can also be achieved by adjusting the parameters for multiple trials and errors. Mixed two-phase method is advantageous for parameter acquisition. Under the same model and dynamics parameters, both DEM-FVM (EDEM-fluent) and SDPH-SPH (LPF^{3D}) coupling methods can better reproduce the motion process and final accumulation range of the Xianchi reservoir landslide (Fig. 16). However, from the perspective of computational efficiency, DEM-FVM will consume more time, which took more than 20 h to simulate the motion of 3000 particles, while the SDPH-SPH coupling

Table 3 Numerical simulation parameters of Xianchi reservoir landslide under different numerical methods

Numerical modeling	Solid phase					Fluid phase		
	Boundary model	Grain size (m)	Dynamic friction factor	Density (kg/m³)	Poisson ratio	Boundary model	Density (kg/m³)	Viscosity factor (Pa·s)
EDEM-fluent (coupled DEM-FVM)	Frictional	3	0.3	2100	0.25	Newtonian fluid	1100	0.017
LPF³ᴰ (coupled SPH-SDPH)		3	0.3	2100	0.25		1100	0.017

Numerical modeling	Equivalent fluid				
	Material	Boundary model	Dynamic friction factor	Density (kg/m³)	Viscosity factor (Pa·s)
DAN3D (SPH/depth-averaged)	Grain	Frictional	0.3	2100	-
	Slurry	Newtonian laminar	-	1100	0.017

(a) DAN3D
(Single-phase grain)

(b) LPF3D
(Single-phase grain)

(c) DAN3D
(Single-phase fluid)

(d) LPF3D
(Single-phase fluid)

Fig. 14 Comparison between full three-dimensional single-phase fluid (LPF³ᴰ) and equivalent fluid model (DAN3D) by depth integration method

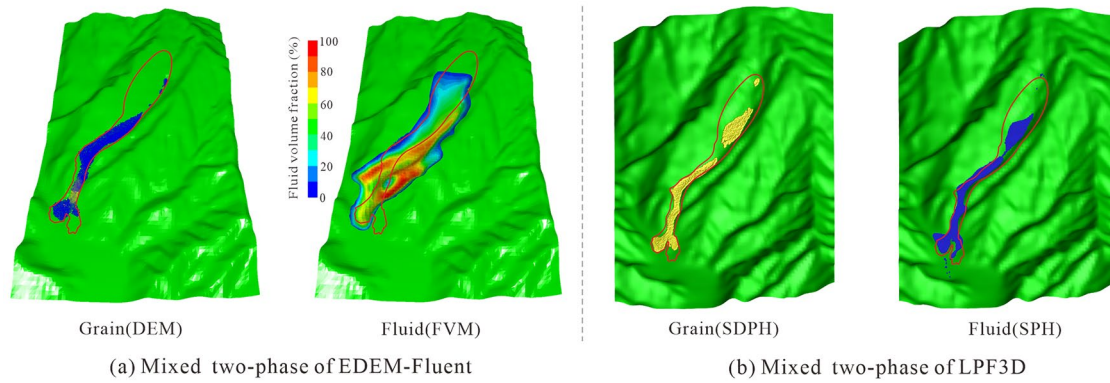**Table 4** Comparison of the single-phase flow simulation results and data

Numerical modeling	Material	Boundary model	Grain size (m)	Maximum velocity (m/s)	Maximum distance (m)	Maximum thickness (m)	Number (Numerical particles)	Result
DAN3D (SPH)	Dry grain	Frictional	-	No movement		20	3000	Figure 14(a)
LPF3D (SDPH)	Dry grain	Frictional	3	Local movement		30	8032	Figure 14(b)
DAN3D (SPH)	Slurry fluid	Newtonian fluid	-	21	1750	20	2000	Figure 14(c)
LPF3D (SPH)	Slurry fluid	Newtonian fluid	-	46	1800	13.9	8032	Figure 14(d)
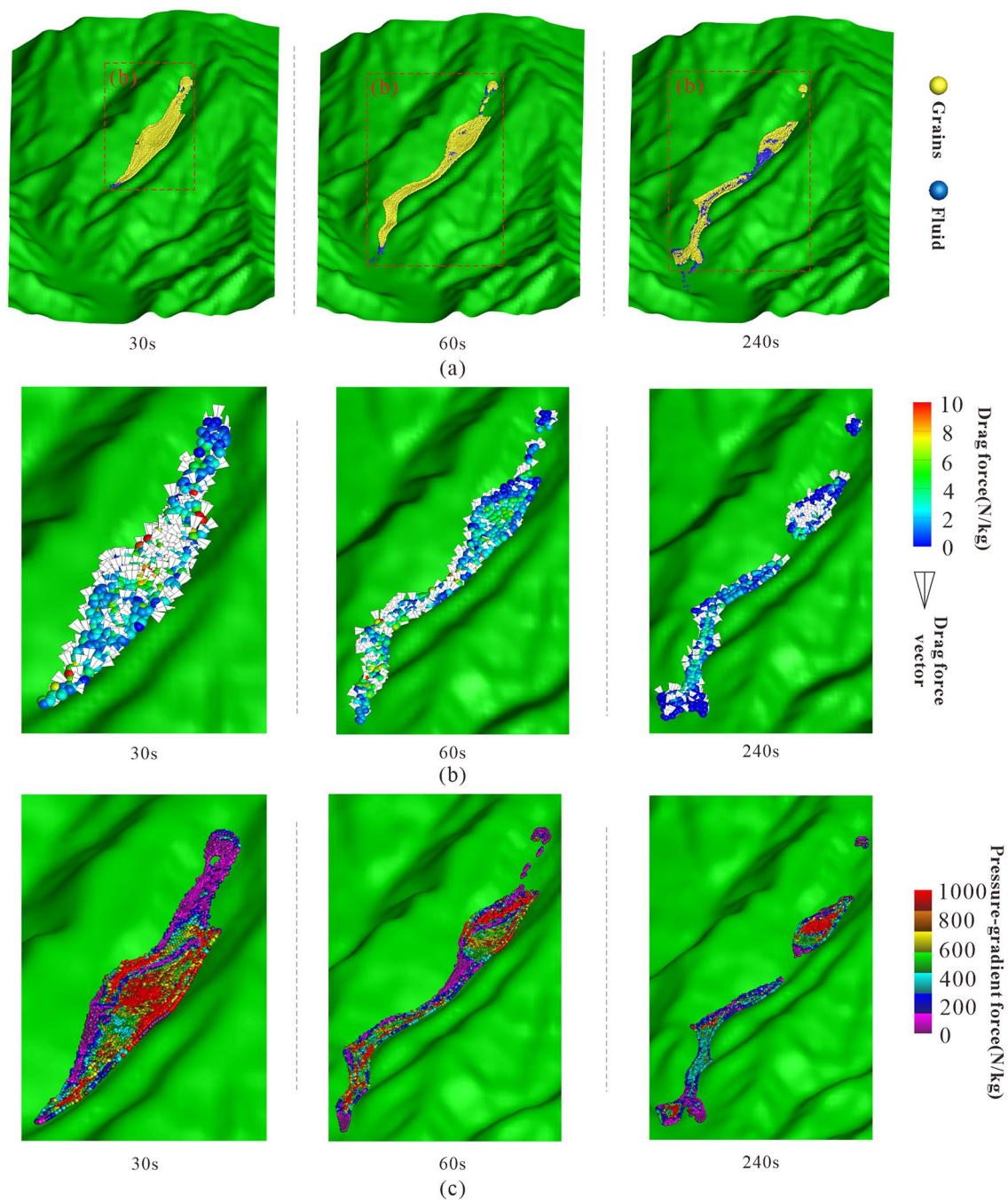
Fig. 15 The numerical simulation result of Xianchi reservoir landslide in full three-dimensional two-phase numerical modeling. **a** Fluid and solid grain accumulation shape with different time stages. **b** Drag force between the solid and the fluid; the direction pointed by the arrow is the direction of the drag force on the solid grains. **c** Distribution of fluid pressure gradient forces on solid grains

(a) Mixed two-phase of EDEM-Fluent   (b) Mixed two-phase of LPF3D

Fig. 16 Comparison of numerical simulation results of different coupling methods

Table 5 Comparison of the solid–liquid two-phase flow simulation results and data

Numerical modeling	Grain size(m)	Maximum velocity (m/s)	Maximum distance (m)	Maximum thickness (m)	Number (Numerical particles)	Computing time (h)
Mixed two-phase flows						
LPF3D (SPH-SDPH)	3	24.6	1550	24.6	16,064	3.5
EDEM-fluent (DEM-FVM)		-	1380	-	3000	20
Actual landslide	1.2–4	-	1600	28	-	

method only used 3.5 h to complete the simulation of 16,000 particles, and the calculated results were basically consistent with the actual accumulation range (Table 5). This method serves as a bridge between continuum-medium algorithms and discrete-medium algorithms based on the same numerical theoretical framework of smoothed particle hydrodynamics (SPH), combines the advantages of granular flow and equivalent fluid algorithms, and improves the simulation efficiency while ensuring accuracy.

Conclusions

Under extreme climate conditions, such as heavy precipitation, glacial lake outbursts, and ice and snow melting, large surface runoff is formed on the motion path of a landslide post-failure. The long runout flow-like landslide has become one of the most disastrous types in China. In this study, a full three-dimensional landslide post-failure numerical computing platform (LPF3D) was proposed. This serves as a bridge between continuum-medium algorithms and discrete-medium algorithms based on the same numerical theoretical framework of smoothed particle hydrodynamics (SPH). This method solved the problem of calculating discrete particles in continuum medium, improved the simulation accuracy by comparing the discrete element method, and can efficiently solve the dynamics process of three-dimensional complex. Solving for the discrete grain phase has been improved as smoothed discrete particle hydrodynamics

(SDPH), which employs the Lagrangian particle method to obtain discrete solutions with low computational cost.

A back-analysis of small-scale flume experiments and landslide cases was performed to verify this numerical modeling of mixed two-phase flow. The parameters and algorithm of numerical modeling were calibrated by experiment results, and the numerical results were almost consistent with the realistic results. Numerical simulation results of LPF3D demonstrate the importance of interaction force and the initial volume fraction of fluid. This water pressure gradient force value acting on solid is larger at certain positions, such as the turning point of the terrain, the leading edge of the sliding main body, and the solid large deposition thickness position. Coupled two-phase method of DEM-FVM, equivalent fluid method of DAN3D, and LPF3D method are used for comparative analysis for Xianchi Reservoir landslide case. Comparison results of different numerical methods show the following: (i) compared with the equivalent fluid method, the simulation results of the motion process and accumulation range of single-phase materials are consistent, and the full three-dimensional details processing accuracy is higher; (ii) compared with coupled two-phase method, the simulation of the motion process and accumulation of two-phase material coupling is basically consistent, and it is less time cost; (iii) LPF3D method combines the advantages of the two algorithms and each individual particle can be traced for force process in this approach.

The numerical computing platform of three-dimensional landslide post-failure (LPF^{3D}) was proposed, which establishes new numerical modeling for solving the two-phase coupling of fluid and solid grains. The new method of LPF^{3D} involving solid–liquid coupling dynamics modeling reflects the actual physical and mechanical processes of long runout landslide motion, and it can be applied for risk assessment and mitigation in the mixed two-phase-flow landslide post-failure (i.e., debris avalanche, debris flow, and debris flood).

Data availability
The data that support the findings of this study are available from the corresponding author upon reasonable request.

Declarations

Competing interest   The authors declare no competing interests.

References

Bowen RM (1980) Incompressible porous media models by use of the theory of mixtures. Int J Eng Sci 18(9):1129–1148

Canelas RB, Crespo AJC, Dominguez JM et al (2016) SPH-DCDEM model for arbitrary geometries in free surface solid-fluid flows. Comput Phys Commun 202:131–140

Chen F, Qiang H, Zhang H et al (2017) A coupled SDPH–FVM method for gas-particle multiphase flow: methodology. Int J Numer Meth Eng 109(1):73–101

Chen F, Yan H (2021) Constitutive model for solid-like, liquid-like, and gas-like phases of granular media and their numerical implementation. Powder Technol 390:369–386

Ergun S (1952) Fluid flow through packed columns. Chem Eng Prog 48:89–94

Evans SG, Guthrie RH, Roberts NJ et al (2007) The disastrous 17 February 2006 rockslide-debris avalanche on Leyte Island, Philippines: a catastrophic landslide in tropical mountain terrain. Nat Hazard 7(1):89–101

Evans SG, Tutubalina OV, Drobyshev VN et al (2009) Catastrophic detachment and high-velocity long-runout flow of Kolka Glacier, Caucasus Mountains, Russia in 2002. Geomorphology 105(3–4):314–321

Fan X, Xu Q, Scaringi G et al (2019) The "long" runout rock avalanche in Pusa, China, on August 28, 2017: a preliminary report. Landslides 16(1):139–154

Gao Y, Li B, Gao H et al (2020) Dynamic characteristics of high-position and long runout landslides in the Emeishan basalt area: a case study of the Shuicheng "7.23" landslide in Guizhou, China. Landslides 17(7):1663–1677

Gao Y, Yin Y, Li B et al (2017) Characteristics and numerical runout modeling of the heavy rainfall-induced catastrophic landslide-debris flow at Sanxicun, Dujiangyan, China, following the Wenchuan Ms 8.0 earthquake. Landslides 14(4):1364–1374

Gao Y, Yin Y, Li B et al (2022) The role of fluid drag force in the dynamic process of two-phase flow-like landslides. Landslides 19(7):1791–1805

Gidaspow D (1994) Multiphase flow and fluidization: continuum and kinetic theory descriptions. Academic press

Gingold RA, Monaghan JJ (1977) smoothed particle hydrodynamics: theory and application to non-spherical stars. Mon Not R Astron Soc 181(3):375–389

Habib R, Gubler MC, Loirat C et al (1975) Dense deposit disease: a variant of membranoproliferative glomerulonephritis. Kidney Int 7(4):204–215

Hungr O (1995) A model for the runout analysis of rapid flow slides, debris flows, and avalanches. Can Geotech J 32(4):610–623

Hungr O, McDougall S (2009) Two numerical models for landslide dynamic analysis. Comput Geosci 35(5):978–992

Ishii M (1975) Thermo-fluid dynamic theory of two-phase flow. NASA Sti/recon Technical Report A 75:29657

Ishii M, Zuber N (1979) Drag coefficient and relative velocity in bubbly, droplet or particulate flows. AIChE J 25(5):843–855

Iverson RM (1997) The physics of debris flows. Rev Geophys 35(3):245–296

Iverson RM (2012) Elementary theory of bed-sediment entrainment by debris flows and avalanches. Geophys Res 117:F03006

Iverson RM, Denlinger RP (2001) Flow of variably fluidized granular masses across three-dimensional terrain: 1. Coulomb mixture theory. J Geophys Res Solid Earth 106(B1):537–552

Iverson RM, LaHusen R (1997) Debris-flow mobilization from landslides. Annu Rev Earth Planet 25:85–138

Jing L, Yang G, Kwok C et al (2019) Flow regimes and dynamic similarity of immersed granular collapse: a CFD-DEM investigation. Powder Technol 345:532–543

Johnson G, Rajagopal KR, Massoudi M (1990) A review of interaction mechanisms in fluid-solid flows

Johnson PC, Nott P, Jackson R (1990a) Frictional-collisional equations of motion for participate flows and their application to chutes. J Fluid Mech 210:501–535

Jop P, Forterre Y, Pouliquen O (2006) A constitutive law for dense granular flows. Nature 441(7094):727–730

Kafui KD, Thornton C, Adams MJ (2002) Discrete particle-continuum fluid modelling of gas-solid fluidised beds. Chem Eng Sci 57(13):2395–2410

Khan AR, Richardson JF (1987) The resistance to motion of a solid sphere in a fluid. Chem Eng Commun 62(1–6):135–150

Kim S, Kamrin K (2020) Power-law scaling in granular rheology across flow geometries. Phys Rev Lett 125(8):088002

Lee CH, Huang Z (2018) A two-phase flow model for submarine granular flows: with an application to collapse of deeply-submerged granular columns. Adv Water Resour 115:286–300

Li B, Gao Y, Yin Y et al (2022) Rainstorm-induced large-scale landslides in Northeastern Chongqing China August 31 to September 2 2014. Bull Eng Geol Environ 81(7):271

Li S, Liu W (2002) Meshfree and particle methods and their applications. Appl Mech Rev 55:1–34

Liu C, Xu Q, Shi B et al (2017) Mechanical properties and energy conversion of 3D close-packed lattice model for brittle rocks. Comput Geosci 103:12–20

Liu W, He S, Chen Z, Yan S, Deng Y (2020) Effect of viscosity changes on the motion of debris flow by considering entrainment. J Hydraul Res 59(1):120–135

Lucy LB (1977) A numerical approach to the testing of the fission hypothesis. Astron J 82(1977):1013–1024

Mencl V (1966) Mechanics of landslides with non-circular slip surfaces with special reference to the Vaiont slide. Géotechnique 16(4):329–337

Midi GDR (2004) On dense granular flows. The European Physical Journal E 14(4):341–365

Monaghan JJ (1994) Simulating free surface flows with SPH. J Comput Phys 110(2):399–406

Mothes PA, Hall ML, Janda RJ (1998) The enormous Chillos Valley Lahar: an ash-flow-generated debris flow from Cotopaxi Volcano. Ecuador Bullet Volcanol 59(4):233–244

Pähtz T, Durán O, De Klerk DN et al (2019) Local rheology relation with variable yield stress ratio across dry, wet, dense, and dilute granular flows. Phys Rev Lett 123(4):048001

Pastor M, Blanc T, Haddad B et al (2015) Depth averaged models for fast landslide propagation: mathematical, rheological and numerical aspects. Arch Comput Methods Eng 22(1):67–104

Pastor M, Tayyebi SM, Stickle MM et al (2021) A depth integrated, coupled, two-phase model for debris flow propagation. Acta Geotech 16(8):2409–2433

Pitman EB, Le L (2005) A two-fluid model for avalanche and debris flows. Philos Trans Royal Soc A: Math Phys Eng Sci 363(1832):1573–1601

Plafker G, Ericksen GE (1978) Nevados Huascarán avalanches. Peru Dev Geotech Eng Elsevier 14:277–314

Pudasaini SP (2012) A general two-phase debris flow model. J Geophys Res Earth Surf 117(F3):F03010

Pudasaini SP, Hutter K (2007) Avalanche dynamics: dynamics of rapid flows of dense granular avalanches. Springer Sci Bus Media

Pudasaini SP, Mergili M (2019) A multi-phase mass flow model. J Geophys Res Earth Surf 124(12):2920–2942

Sassa K (1989) Geotechnical model for the motion of landslides//Proc. 5th Inter. Symp on Landslide 1:37–56

Sassa K (1994) Development of a new cyclic loading ring-shear apparatus to study earthquake-induced-landslides. Report for Grain-in-Aid for Developmental Scientific Research by the Ministry of Education Science and Culture Japan (Project No. 03556021) 106

Savage SB, Hutter K (1989) The motion of a finite mass of granular material down a rough incline. J Fluid Mech 199:177–215

Savage SB, Hutter K (1991) The dynamics of avalanches of granular materials from initiation to runout. Part I: Analysis Acta Mechanica 86(1–4):201–223

Savage SB, Iverson RM (2003) Surge dynamics coupled to pore-pressure evolution in debris flows//Proc. 3rd Int. Conf. on Debris-Flow Hazards Mitigation: Mechanics, Prediction, and Assessment, Davos, Switzerland, edited by: Rickenmann, D. and Chen, CL, Millpress, Rotterdam: 503–514

Shan T, Zhao J (2014) A coupled CFD-DEM analysis of granular flow impacting on a water reservoir. Acta Mech 225(8):2449–2470

Shen Z, Wang G, Huang D, Jin F (2022) A resolved CFD-DEM coupling model for modeling two-phase fluids interaction with irregularly shaped particles. J Comput Phys 448:110695

Shu A, Wang S, Rubinato M, Wang M, Qin J, Zhu F (2020) Numerical modeling of debris flows induced by dam-break using the smoothed particle hydrodynamics (SPH) method. Appl Sci 10(8):2954

Si P, Shi H, Yu X (2018) Development of a mathematical model for submarine granular flows. Phys Fluids 30(8):083302

Singh J, Catsoulis S, Lakehal D, Narayanan C (2023) Predicting pressure-drop for pseudo-homogeneous slurry flows using the mixture model at high solids concentrations. Int J Multiph Flow 159:104339

Stokes GG (1851) On the effect of the internal friction of fluids on the motion of pendulums. Trans Cambridge Philos Soc Part II 9:8–106

Takarada S, Ui T, Yamamoto Y (1999) Depositional features and transportation mechanism of valley-filling Iwasegawa and Kaida debris avalanches. Japan Bullet Volcanol 60(7):508–522

Tan H, Chen S (2017) A hybrid DEM-SPH model for deformable landslide and its generated surge waves. Adv Water Resour 108(oct): 256–276

Tan H, Xu Q, Chen S (2018) Subaerial rigid landslide-tsunamis: Insights from a block DEM-SPH model. Eng Anal Bound Elem 95(oct): 297–314

Tayyebi SM, Pastor M, Stickle MM (2021) Two-phase SPH numerical study of pore-water pressure effect on debris flows mobility: Yu Tung debris flow. Comput Geotech 132(2):103973

Tayyebi SM, Pastor M, Stickle MM et al (2022) SPH numerical modeling of landslide movements as coupled two-phase flows with a new solution for the interaction term. Eur J Mech-B/fluids 96:1–14

Topin V, Dubois F, Monerie Y, Perales F, Wachs A (2011) Micro-rheology of dense particulate flows: Application to immersed avalanches. J Nonnewton Fluid Mech 166(1–2):63–72

Truesdell C, Truesdell C (1984) Historical introit the origins of rational thermodynamics. Springer, New York

Voellmy A (1955) Uber die Zerstorungskraft von Lawinen. Schweizerische Bauzeitung Jahrg 73: 159–162, 212–217, 246–249, 280–285 (in German)

Voight B, Janda RJ, Glicken H et al (1983) Nature and mechanics of the Mount St Helens rockslide-avalanche of 18 May 1980. Geotechnique 33(3):243–273

Wen C, Yu Y (1966) A generalized method for predicting the minimum fluidization velocity. AIChEJ 12(3):610–612

Xing A, Yuan X, Xu Q et al (2017) Characteristics and numerical runout modeling of a catastrophic rock avalanche triggered by the Wenchuan earthquake in the Wenjia valley, Mianzhu, Sichuan. China Landslides 14(1):83–98

Yamada M, Mangeney A, Matsushi Y et al (2018) Estimation of dynamic friction and movement history of large landslides. Landslides 15(10):1963–1974

Yin Y, Sun P, Zhang M et al (2011) Mechanism on apparent dip sliding of oblique inclined bedding rockslide at Jiweishan, Chongqing. China Landslides 8(1):49–65

Yin Y, Cheng Y, Liang J et al (2016) Heavy-rainfall-induced catastrophic rockslide - debris flow at Sanxicun, Dujiangyan, after the Wenchuan Ms 8.0 earthquake. Landslides 13(1): 9–23

Yin Y, Li B, Gao Y et al (2023) Geostructures, dynamics and risk mitigation of high-altitude and Long runout rockslides. J Rock Mech Geotech Eng 15(1):66–101

Zhao L, Liu X, Mao J et al (2020) Three-dimensional distance potential discrete element method for the numerical simulation of landslides. Landslides 17:361–377

Yang Gao · Bin Li (✉) · Jun Li
Institute of Geo-Mechanics, Chinese Academy of Geo-Sciences, CGS, Beijing, China
Email: libin1102@163.com

Yang Gao · Bin Li Jun Li
Key Laboratory of Active Tectonics and Geological Safety, Ministry of Natural Resources, Beijing, China

Han Zhang · Weile Wu
Changan University, Shannxi, China

Yueping Yin
China Institute of Geo-Environment Monitoring, Beijing, China